Journal of Materials Chemistry C

ROYAL SOCIETY OF CHEMISTRY

PAPER

View Article Online
View Journal | View Issue

Check for updates

Cite this: J. Mater. Chem. C, 2024, 12, 8473

Establishing the correlation of negative permittivity and AC conductivity of $La_{2-x}Sr_xNiO_4$ (x = 0, 0.1, 0.3, 1.0) for microwave shielding applications

Tarun Katheriya,[a] Gurudeo Nirala[ab] and Shail Upadhyay *[a]

Negative permittivity, a phenomenon observed in certain materials, has attracted considerable interest because of its significant implications in various fields of physics and engineering. Herein, from the perspective of intrinsic properties of single-phase materials, a few compositions of the $La_{2-x}Sr_xNiO_4$ system (x = 0, 0.1, 0.3, 1.0) were synthesized using the solid-state reaction method. XRD studies showed that the solubility limit of Sr in the lattice of La_2NiO_4 is limited ($0.3 < x < 1.0$). Morphological studies have revealed that average grain size and density increase with increasing Sr content. Dielectric/electrical properties were studied across a wide frequency range (20 Hz–2 MHz) and at higher temperatures (30–600 °C). All the samples have negative dielectric constant and this is attributed to plasma oscillation. The Drude model was fitted to experimental data and parameters like plasma frequency (ω_p) and relaxation frequency (ω_τ) were determined. The low value of activation energy (<0.05 eV) for direct current (D.C.) conduction and an increasing trend in relaxation time (τ) with temperature suggest a "small-polaron hopping conduction" mechanism. Studies on complex plane impedances have shown positive reactance and increased inductance with Sr-doping. Microwave shielding analysis revealed reflection as the primary shielding mechanism. The composition with x = 0.30 having high dielectric constant and conductivity shows the best shielding capabilities. These findings highlight the ability to tune the negative dielectric properties of La_2NiO_4 through compositional adjustments, which is significant for applications such as microwave shielding and coil-less inductive materials for future devices.

Received 5th January 2024,
Accepted 27th March 2024

DOI: 10.1039/d4tc00064a

rsc.li/materials-c

Published on 16 May 2024. Downloaded on 7/22/2025 2:32:36 PM.

1. Introduction

Negative permittivity materials belong to the class of metamaterials, which are artificially engineered materials exhibiting some unique properties not present in natural materials. They can influence electromagnetic waves in ways that ordinary materials cannot.[1–4] Earlier, properties of metamaterials were controlled by engineering complex geometric structures, rather than depending merely on material composition and microstructure. Many efforts have been made so far to realize negative permittivity in real materials so that properties can be controlled by compositional modifications and microstructure. A review article published in 2021 by Kai *et al.* highlighted the latest developments in the field of negative permittivity in composites called metacomposites.[5] The negative permittivity in these composites appears when the concentration of metals exceeds a specific threshold, creating a percolating conducting path. However, these composites have limitations in low-dimensional applications, mainly due to their heterogeneous and non-uniform composition. To address these limitations, researchers have shifted their focus toward exploring negative permittivity in homogeneous or single-phase materials. Negative permittivity has been reported in various single-phase materials: Sr-doped $LaMnO_3$,[6–8] Mn-doped Sr_2SnO_4,[9] Nb-doped Sr_2MnO_4,[10] Sb-doped SnO_2,[11] and Sn-doped In_2O_3.[12] We have put continuous efforts into exploring single-phase materials to achieve negative permittivity at room temperature in pristine (undoped) compounds. We have recently observed negative permittivity at and above room temperature in La_2NiO_4.[13]

La_2NiO_4 nickelate with the K_2NiF_4-type structure is an important dielectric material that has received increasing attention due to its application as cathode material in solid oxide fuel cells (SOFCs).[14–17] There is growing interest among researchers in exploring its dielectric and electrical conductivity properties for other applications such as microwave shielding. It is reported that Sr doping at the La site can modify the

[a] Department of Physics, Indian Institute of Technology (BHU), Varanasi-221005, India
[b] Department of Basic Science and Humanities, Government Polytechnic, Munger 811213, India. E-mail: supadhyay.app@itbhu.ac.in

Published on 16 May 2024. Downloaded on 7/22/2025 2:32:36 PM.

electrical and dielectric characteristics of La_2NiO_4. This highlights the fundamental role of the dielectric response and electrical conductivity of La_2NiO_4 in influencing its microwave shielding capabilities.[18] While current reports mostly focus on measuring the electrical properties of materials at low temperatures and their microwave shielding properties at very high frequencies (GHz), it is acknowledged that, for most device applications, the properties of materials should be characterized at and above room temperature.

The aforementioned gap has motivated us to conduct a systematic detailed experimental investigation to understand the effect of Sr-doping on the structural, micro-structural, electrical properties, dielectric properties, and microwave shielding properties of La_2NiO_4. To achieve the objective, compositions with x = 0, 0.1, 0.3, and 1.0 of the system $La_{2-x}Sr_xNiO_4$ have been synthesized by the solid-state reaction method. The dielectric and electrical properties of the synthesized samples have been studied in the radio-frequency range (20 Hz–2 MHz) and a wide temperature range (RT–600 °C) using an LCR meter. Microwave shielding effectiveness has been measured in two different frequency bands of 1–2 MHz and 8–13 GHz.

2. Sample preparation

The compositions with x = 0, 0.1, 0.3, and 1.0 of $La_{2-x}Sr_xNiO_4$ were synthesized by the solid-state reaction method. For convenience, these compositions have been referred to by code name LN0 (x = 0.0), LN1 (x = 0.1), LN2 (x = 0.3) and LN3 (x = 1.0) henceforth. Spectroscopically pure La_2O_3 (Alfa Assar, purity >99.9%), $NiCO_3{\cdot}2Ni(OH)_2{\cdot}xH_2O$ (Sigma Aldrich, purity >99.9%) and $SrCO_3$ (Alfa Assar, purity > 99.9%) were taken in a stoichiometric ratio and crushed in a planetary ball mill (Retsch PM 200, Germany) using an agate jar and balls (milling vessel is 250 ml, and the diameter of the balls is 10.2 mm) for 15 h at 200 rpm taking acetone as the mixing medium. During the mixing period, a ball-to-powder ratio of 5 : 1 (by weight) was fixed. To prevent the heating and sticking of the powder to the container walls and balls, and agglomeration, the milling sequence was selected, such as 15 min of milling followed by 5 min of stop period. The prepared mixtures were dried for a long period (24 h) at 80 °C in a conventional oven. The calcination of the mixtures was performed at 1200 °C (optimized) in a platinum crucible for 12 h in an ambient atmosphere. The powders thus obtained were reground with 2% PVA, pressed into cylindrical pellets (10.0 × 2.0 mm), and sintered at 1500 °C for 12 h with the heating rate of 4 °C min^{-1} and 2 °C min^{-1} in cooling.

For the microwave shielding measurement, the powder of sintered pellets was dispersed in clear epoxy and dried overnight. The weight ratio of powder/epoxy for each composite was maintained at 4 : 1 (each sample contained 80 wt% powder). The samples were cut into the desired rectangular shape waveguide adapters.

3. Characterization

The phase purity of the samples was confirmed by recording the X-ray diffraction pattern using CuK_α (λ = 1.5406 Å) radiation with the help of a diffractometer (Rikagu X'PERT PRO MPD). The room temperature XRD patterns were collected in the range of 20–80° with a step size of 0.02°. The structure was analyzed by the Rietveld refinement method using the ''FullProf program'' and a pseudo-Voigt profile function with preferred orientation correction. The microstructure was studied by using a bench-top scanning electron microscope (Nova Nano SEM450, USA) at room temperature. The dielectric and electrical properties of the samples were investigated and measured using an inductance–capacitance–resistance (LCR) meter (Keysight E-4980A, USA) in a wide range of temperature (40–600 °C) and frequency (20 Hz–2 MHz) with a heating rate of 4 °C min^{-1} in cooling. Silver wires were used as electrodes in the sample holder. Conducting paste was not applied on the surface of the pellets for electrical measurements, as the samples were already conducting. Valence states of the constituent elements La, Sr, Ni, and O were studied by recording the core spectra of these elements employing an X-ray photoelectron spectrometer (Thermo Fisher Scientific K-Alpha, USA), operating at a high pressure of 5 × 10^{-11} Torr.

Rectangular-shaped samples (length a = 23.86 mm and width b = 10.05 mm) were fit into the wave-guide adapter, with the whole assembly connected to a vector network analyzer (Agilent N5230c, USA) using co-axial cables for microwave property measurements. Full two-port calibration was performed to remove errors. Two coaxial rectangular wave-guide adapters, filling the fixture cross-section, were used to determine the S-parameters and study the microwave shielding properties of undoped and doped La_2NiO_4, *i.e.* LN0, and LN2, for comparative study.

4. Results and discussion

4.1. Phase analysis and crystal structure

It is well known that calcination temperature has a determinant role in the phase purity and morphology of the powders. Mixtures of raw materials were subjected to calcination at 1200 °C for 8 h. The room temperature diffraction pattern of calcined powders was recorded and is shown in Fig. 1(a). The peaks observed in the XRD pattern of the samples have been indexed using the COD (crystallographic open database) file (1533571) of La_2NiO_4. Apart from the La_2NiO_4 peaks, there are a few peaks of very low intensities of raw materials, and a peak of secondary phase $LaNiO_3$ was also observed (at 32°). To eliminate the impurity phases and get the desired single-phase materials, pellets of calcined powders were obtained using a stainless steel die and a hydraulic press.

Pellets made from the calcined powders were sintered at 1500 °C for 12 h. Sintered pellets were cleaned and polished, and their diffraction pattern is shown in Fig. 1(b). Upon comparison with the COD file 1533571 (for La_2NiO_4), it was found that the peaks corresponding to raw materials and

 This journal is © The Royal Society of Chemistry 2024

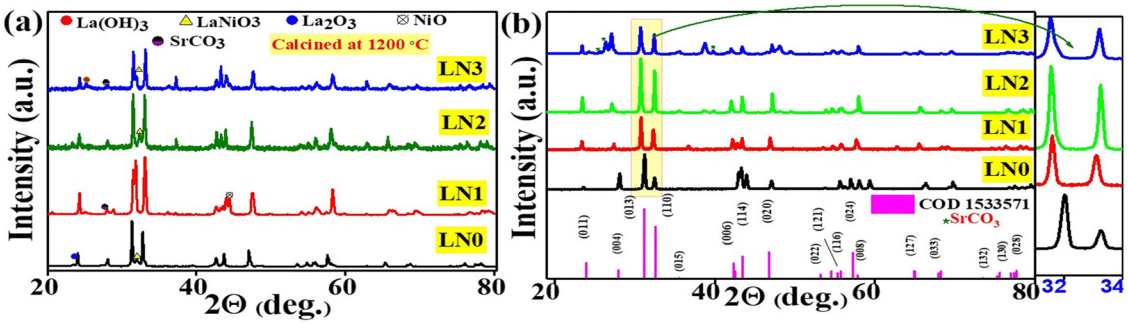

Fig. 1 X-ray diffraction patterns of samples LN0–LN3: (a) calcined powders and (b) sintered pellets. In the inset, the magnified view of the highest-intensity peaks is shown.

Published on 16 May 2024. Downloaded on 7/22/2025 2:32:36 PM.

Table 1 Parameters obtained from the Rietveld refinement process

S.N.	Composition	Sample code	Lattice parameters (Å)	c/a	Volume (Å^3)	Density $\rho_{theoretical}$ (g cm^{-3})
1	La_2NiO_4	LN0	$a = b = 3.851$ $c = 12.589$	3.269	186.697	6.934
2	$La_{1.9}Sr_{0.1}NiO_4$	LN1	$a = b = 3.855$ $c = 12.671$	3.286	188.304	7.135
3	$La_{1.7}Sr_{0.3}NiO_4$	LN2	$a = b = 3.866$ $c = 12.729$	3.292	190.247	7.228
4	$LaSrNiO_4$	LN3	$a = b = 3.867$ $c = 12.719$	3.289	190.196	6.955

secondary phases have disappeared. Only the peaks of La_2NiO_4 are present, except for the composition with x = 1.0 (LN3).

In sample LN3 (x = 1.0), impurity peaks of very low intensity of $SrCO_3$ suggest that the solubility limit of Sr in the lattice of $La_{2-x}Sr_xNiO_4$ solid solution is $x < 1.0$ under the chosen experimental parameters.

We used the 'FullProf suite Programme' to analyze X-ray diffraction patterns using the Rietveld refinement method to determine lattice parameters. For comparing the form of diffraction peaks, we used the pseudo-Voigt function. Furthermore, the background is represented by interpolation between collections of background points up to refinable heights. Throughout the process of refinement, important variables were methodically improved. A number of variables have been refined, including lattice dimensions (a, b, c), thermal attributes (B), scale factor, background properties, half-width parameters, zero correction, and positional coordinates (x, y, z) while the occupancy parameters of all ions remained constant during the process of refinement. For the refinement, a tetragonal crystal structure within the space group ($I4/mmm$) as reported for La_2NiO_4 was adopted. In this structure, La/Sr atoms are situated at the 4e (0, 0, z) sites, oxygen atoms O1 and O2 occupied positions at 4c (0.5, 0, 0) and (0, 0.5, 0), and Ni atoms at the 2a (0, 0, 0) position. The refinement pattern was in good agreement with the calculated and experimental diffraction patterns as reported previously.[19] The structural parameters obtained after final refinement are presented in Table 1.

From Table 1 it is noticed that the lattice parameters increase with increasing doping concentration, *i.e.* x. A linear increase in unit cell volume is also observed. A magnified view of the most intense diffraction peaks (013) and (110) is shown in the inset of Fig. 1(b). The position of the peaks shifts towards lower angles with increasing doping concentration (x). This shift signifies an expansion of the unit cell. The reason for the expansion of unit cell volume lies in the comparison of atomic radii of dopant Sr^{2+} and host La^{3+} in the same coordination number. The ionic radius of Sr^{2+} is 1.31 Å whereas that of La^{3+} is 1.06 Å. Due to the larger atomic radius of Sr^{2+} in comparison to La^{3+}, the incorporation of Sr^{2+} ions in the lattice of La_2NiO_4 at the La^{3+} ion's site leads to an expansion in the unit cell volume. This result becomes evident through the shift of the diffraction peak towards lower angles, as clearly demonstrated in Fig. 1(b).

For perovskite structures, Goldschmidt's tolerance factor, denoted as "t", is an indicator of the stability and distortion of crystal structures. The tolerance factor, for A_2BO_4 structures, is defined as follows:[9]

$$t = \frac{r_A + r_o}{\sqrt{2}(r_B + r_o)} \quad (1)$$

We have calculated the tolerance factor using eqn (1). In the $La_{2-x}Sr_xNiO_4$ system, the tolerance factor is found within the range of 0.88 (LN0) to 0.97 (LN3), increasing with increasing Sr doping concentration.

Published on 16 May 2024. Downloaded on 7/22/2025 2:32:36 PM.

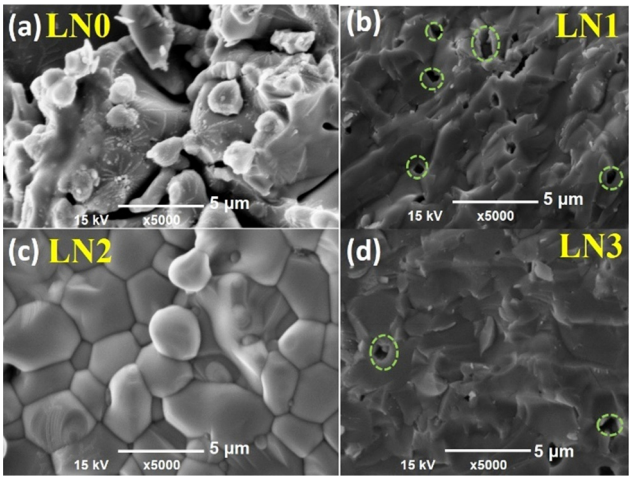

Fig. 2 SEM images of fractured surfaces of sintered pellets. The amount of Sr-dopant for (a)–(d) is 0, 0.1, 0.3, and 1.0 respectively.

4.2. Microstructure analysis

The microstructure and surface morphology of sintered pellets were examined using a bench-top scanning electron microscope (BT-SEM). Fig. 2(a–d) display micrographs of the fractured surfaces at a magnification of 5000×. These micrographs reveal the presence of well-developed grains with cuboidal shapes. Materials of the RP (rock salt and perovskite) type have a unit cell structure in which one dimension, responsible for the stacking of perovskite [ABO_3] and rock salt [A–O] structures, is longer than the other two dimensions. In the lattice of the current RP phase of $La_{2-x}Sr_xNiO_4$, anisotropic thermal expansion is evident, resulting in varying degrees of dilation along different axes, with a more pronounced expansion along the *c*-axis. This behavior is attributed to the structural diversity of the material. Consequently, the sintering process, involving thermal cycling, can lead to a combination of grain development and anisotropic modifications, potentially resulting in the formation of micro-pores.[20,21] From samples LN1 to LN3, upon Sr substitution, there is a significant reduction in pore size, leading to improved structural density and denser ceramics. We have calculated the experimental densities of sintered samples at room temperature with the help of a pycnometer (25 ml capacity), using Archimedes' principle. The experimental densities for x = 0, 0.1, 0.3, and 1.0 samples were 89.7% (±0.023%), 91.2% (±0.061%), 93% (±0.049%), and 92.7% (±0.095%) respectively. The density values may initially appear similar, however, a visible increase is evident upon incorporation of Sr.

5. Electrical properties

The variation in the negative permittivity in Sr-doped lanthanum nickelate ($La_{2-x}Sr_xNiO_4$) with changes in temperature and frequency can be understood and explained by analyzing various electrical parameters such as conductivity (σ_{total}), permittivity (ε'_r), conduction-loss (ε''_c), and impedance (Z), along with calculated parameters such as carrier concentration (n_{eff}) and plasma frequency (ω_p). We have described these parameters in detail in the following sections.

5.1. Negative dielectric constant

The relative permittivity or dielectric constant (ε'_r) of the samples was measured over a wide range of temperatures, from 30 °C to 600 °C, and frequencies ranging from 20 Hz to 2 MHz as shown in Fig. 3(a–d). It has been observed that the absolute value of the dielectric constant increases with increasing temperature up to a certain point, after which it decreases for all samples. This temperature, where the trend changes, is known as the transition temperature. Additionally, with increasing Sr doping concentration (x), the transition temperature decreases. For the undoped LNO sample (x = 0), the transition temperature was found to be 450 °C. However, in the LN2 sample (x = 0.3), the transition temperature has significantly dropped to 230 °C. In contrast, the magnitude of the dielectric constant increases with increasing doping concentration. These findings demonstrate the influence of Sr doping on the dielectric properties of La_2NiO_4. In Fig. 3(d) this influence can be further verified by re-plotting the dielectric constant with temperature at a frequency of 1 kHz, which shows a clear trend of decreasing transition temperature with increasing Sr doping. In addition, as the temperature rises, we observe an increase in the dispersion of ε'_r (real part of permittivity) with frequency. This trend closely resembles previously reported observations, indicating that the temperature-dependent variations in dielectric constant and dispersion are inherent characteristics of the samples and are not attributable to any artifacts stemming from the sample-electrode contribution.

In prior studies, two theoretical models, namely the Drude and Drude–Lorentz models, have been used to fit the experimental data concerning negative permittivity. Researchers have mostly used the Drude model to elucidate the behavior of negative permittivity in metals and semiconductors.[22,23]

According to this model, the real part of the complex permittivity (ε'_r) is expressed as (2)

$$\varepsilon'_r = 1 - \frac{{\omega_p}^2}{{\omega_\tau}^2 + \omega^2} \quad (2)$$

In this equation, ω_τ represents the damping factor, which signifies the collision frequency of electrons. On the other hand, ω_p stands for the Drude plasma frequency,[11] and it is correlated to parameters such as carrier concentration (n_{eff}), effective mass (m^*), and electronic charge (e) as indicated below:

$$\omega_p = \sqrt{\frac{n_{eff} \cdot e^2}{m^2 \cdot \varepsilon_0}} \quad (3)$$

The Drude model (eqn (2)) was fitted to the experimental data points shown in Fig. 3(a–c). The solid line represents the data generated by eqn (2), while the symbols are the experimental data points. The fitting curves closely align with the experimental data points, indicating a good agreement between

 This journal is © The Royal Society of Chemistry 2024

Published on 16 May 2024. Downloaded on 7/22/2025 2:32:36 PM.

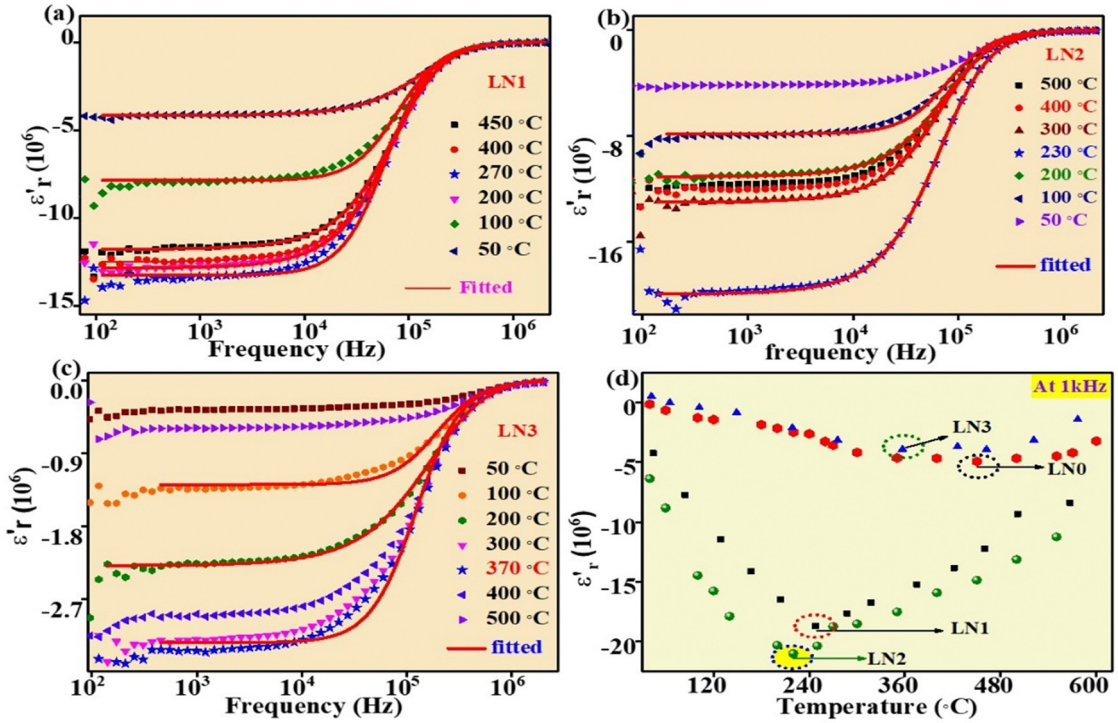

Fig. 3 (a)–(c) Variation of real permittivity with frequency for (a) LN1, (b) LN2, and (c) LN3 at representative temperatures, fitted with the Drude model. (d) Variation of real permittivity with temperature at 1 kHz.

the experimental and theoretical data points. This suggests that negative permittivity arises from the plasma oscillation of free (delocalized) electrons, a phenomenon typically observed in metals and semiconductors. The values of ω_τ and ω_p obtained through the fitting process at various temperatures are given in Table 2.

In the Drude model, ω_τ is related to relaxation time, τ ($\omega = 2\pi$, $f = 2\pi/\tau$), of the charge carriers. In metals, ω_τ increases (τ decreases) with temperature, *i.e.* it leads to an increase in resistance as temperature rises. However, for the synthesized samples, ω_τ is decreasing (τ is increasing) with increasing temperature. The mobility of the electrons is directly proportional to the relaxation time of the electron. The increasing value of τ with temperature indicates an increase in mobility with temperature. In the case of band conduction, mobility decreases with increasing temperature, whereas in the case of hopping conduction, mobility (μ) increases with increasing temperature. Thus, a decreasing value of ω_τ with increasing temperature suggests hopping-type conduction in the samples.

With the presumption that $m^* = m$, the values of n_{eff} were computed by applying eqn (3) and are given in Table 2. The value of n_{eff} is found to increase slowly as the amount of doping increases. An increase in n_{eff} eventually leads to an increase in conductivity. The conduction loss (ε_c'') is related to direct current conductivity (σ_{dc}) by the relation $\varepsilon_c'' = \sigma_{dc}/\omega\varepsilon_o$. At room temperature, the variation of ε_c'' against frequency for samples is shown in Fig. 4. We can see that on increasing Sr concentration, ε_c'' increases.

Table 3 summarizes the value of ε_c'' at two different frequencies. The values reported in Table 3 are approximately 5 orders by magnitude higher than the values reported in the literature.[4] Cheng *et al.* reported strong electromagnetic shielding

Table 2 Parameters obtained from fitting the Drude model to permittivity data

	LN1			LN2			LN3		
T (°C)	ω_τ (MHz)	ω_P (GHz)	n_{eff} (m^{-3})	ω_τ (MHz)	ω_P (GHz)	n_{eff} (m^{-3})	ω_τ (MHz)	ω_p (GHz)	n_{eff} (m^{-3})
50	1.586	20.36	$\sim 1.72 \times 10^{17}$	1.359	23.69	$\sim 1.92 \times 10^{17}$	2.601	24.65	$\sim 2.11 \times 10^{17}$
100	1.382	20.72		0.940	24.66		2.457	24.4	
150	1.177	21.72		0.796	24.60		2.298	25.11	
200	0.986	21.77		0.736	22.71		1.870	24.77	
250	0.816	22.15		0.731	22.42		1.664	22.44	
300	0.803	22.35		0.730	22.37		1.560	22.51	
350	0.851	22.18		0.756	22.21		1.4.95	21.7	
400	0.869	21.07		0.768	22.24		1.444	20.40	
500	1.002	21.43		0.899	22.14		1.513	26.32	
600	1.072	20.01		1.242	22.65		1.560	26.19	

Published on 16 May 2024. Downloaded on 7/22/2025 2:32:36 PM.

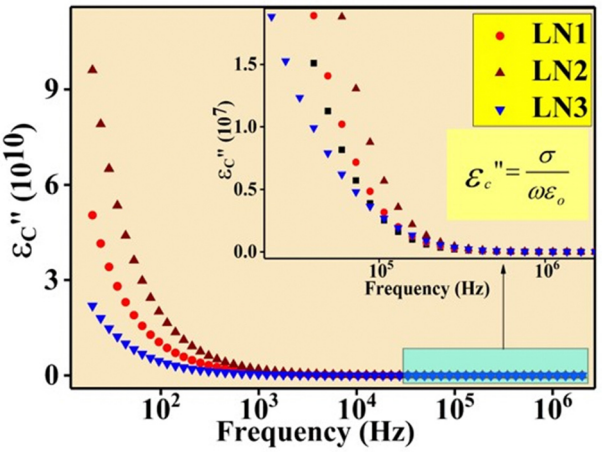

Fig. 4 Variation of ε_c'' with frequency with varying Sr content at room temperature.

Table 3 Room temperature conduction loss (ε_c'') for different compositions at two different frequencies

	Frequency	
Samples	1 kHz	1 MHz
LN1	0.6×10^{10}	2×10^7
LN2	11×10^{10}	7×10^7
LN3	3×10^{10}	2.1×10^7

properties in carbon/Si_3N_4 due to huge impedance mismatching caused by the high value of negative permittivity and dielectric loss.[24,25] High values of ε_r' and ε_c'' make these materials suitable for electromagnetic shielding and microwave absorption applications.

The observed values of ε_c'' mentioned in Table 3 are further confirmed by the study of electrical conductivity, discussed in the subsequent section.

5.2. Electrical conductivity

AC conductivity (σ_{ac}) has been calculated using the measured values of capacitance (C) and dissipation factor (D) in the temperature and frequency ranges that are mentioned above. The relationship between σ_{ac} and frequency at some distinct temperatures is presented in Fig. 5(a–c). At low frequencies (up to 100 kHz), σ_{ac} remains constant and independent of frequency. However, at higher frequencies, σ_{ac} diminishes with increasing frequency. This phenomenon is primarily attributed to the skin effect observed, particularly in metallic materials. The skin effect is a phenomenon that arises at high frequencies, in which alternating current (AC) mostly flows in the outermost layer of a conductor. As the frequency increases, resistance also increases. This happens as a consequence of the AC-inducing self-generated magnetic fields, which lead to electron concentration close to the surface of the conductor. Hence, at higher frequencies, electric current flows near the surface of the conductor. This results in an increase in resistance and a decrease in the effective cross-sectional area available for current conduction. The penetration of the current at the surface is known as the "skin depth". The skin depth is inversely proportional to the square root of the frequency and directly proportional to the square root of the resistivity of the material.

According to the Drude model, AC conductivity of metals can be expressed as[13]

$$\sigma_{ac} = \sigma_{dc}\frac{\omega_\tau{}^2}{\omega^2 + \omega_\tau{}^2} \quad (4)$$

By fitting eqn (4) to the experimental points in Fig. 5, we have determined the values of DC conductivity (σ_{dc}) and ω_τ at different temperatures for all the samples. These results are shown in Table 4.

From Table 4 it is clear once again that ω_τ decreases with increasing temperature as reported in Table 3. DC conductivity increases with increasing temperature up to a particular temperature (transition temperature) and above this temperature it starts decreasing. Every composition displays an obvious transition in electrical conduction characteristics from semiconductor-type to metal-type, which is similar to previously reported results.[26] The electrical conductivity increases with measuring temperature through a maximum transition temperature and then decreases with the further increase of temperature.

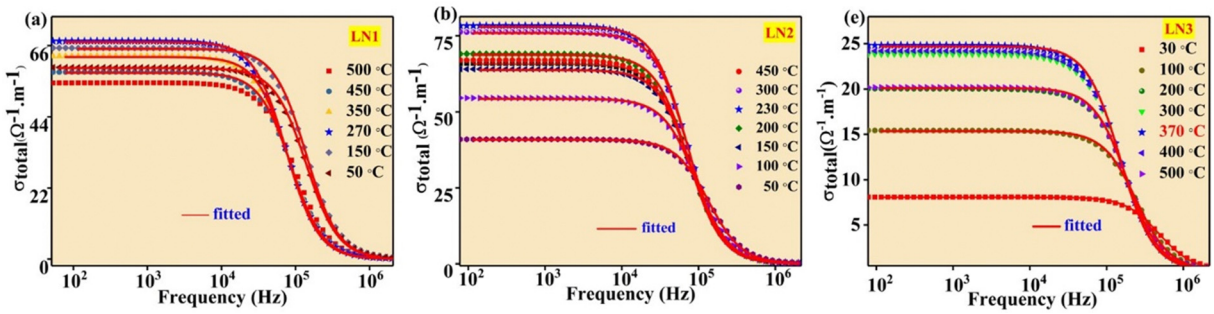

Fig. 5 (a–c) Variation of electrical conductivity of samples with frequency at different temperatures. The skin effect is observed at high frequencies ($>10^4$ Hz), indicating a non-uniform current distribution through the sample's cross-section. LN2 exhibits the highest electrical conductivity ($\sim$79 Ω^{-1} m^{-1}).

 This journal is © The Royal Society of Chemistry 2024

Published on 16 May 2024. Downloaded on 7/22/2025 2:32:36 PM.

Table 4 Fitting parameters obtained from the Drude model for AC conductivity

	LN1		LN2		LN3	
Temperature (°C)	σ_{dc} (S m^{-1})	ω_τ (MHz)	σ_{dc} (S m^{-1})	ω_τ (MHz)	σ_{dc} (S m^{-1})	ω_τ (MHz)
100	62	0.837	54	0.98	17	2.54
200	67	0.705	77	0.94	21	2.29
300	66	1.44	75	0.799	24	1.87
400	65	0.869	70	0.760	23	1.74
500	63	1.38	64	0.898	20	1.55

In Fig. 6, a graph depicting the log of σ_{dc} plotted against $1000/T$ shows a linear increase in $\log\sigma_{dc}$ with the inverse of temperature. This linear behaviour suggests that conductivity obeys the Arrhenius relation as given below:

$$\sigma_{dc} = Ae^{-E_a/k_BT} \quad (5)$$

where A represents the pre-exponential factor, E_a denotes the activation energy for DC conduction, k_B is the Boltzmann constant, and T denotes the absolute temperature in kelvin (K).

For all compositions, using linear fitting of the measured data (below the transition temperature) the value of the slope was computed, and hence the activation energy. The value of the activation energy for all the samples is shown in their respective plot. The value of activation energy, *i.e.*, the energy needed for the charge carrier to pass through the energy barriers caused by the defects, was minimum for sample LN2 and maximum for LN3. The observed activation energy aligns with values reported by other researchers, suggesting that the "small-polaron hopping mechanism" may be possible in La_2NiO_4 oxide.[27,28] For the composition LN2, we have observed the maximum conductivity of about $\sim$79 Ω^{-1} m^{-1} at 230 °C (transition temperature) which is at least three times higher than that of the undoped LN0. A similar behavior is observed for other compositions as well at different transition temperatures, confirming the intrinsic behavior of Sr doped and undoped layered lanthanum necklets.

According to defect chemistry, the replacement of La by a lower valence element such as Sr would result in either the generation of electron/holes at the nickel site or the change in oxygen content or change in the valence state of nickel,[20,29] as described by the below equations:

$$La_{La}^{X} = La_{Sr}' + h \quad (6)$$

$$2La_{La}^{X} = 2La_{Sr}' + V_o^{\bullet} \quad (7)$$

$$La_{La}^{X} = La_{Sr}' + Ni_{Ni}^{\bullet} \quad (8)$$

It is reported that La_2NiO_4 is a p-type conductor.[27] If charge compensation occurs according to eqn (6), doping of Sr will generate more charge carriers, and hence conductivity will increase. On the other hand, a decrease in the activation energy with increasing Sr content is possible due to an increase in the number of hopping sites. An increase in the hopping sites may be possible on partial oxidation of Ni^{2+} to Ni^{3+}.

6. XPS analysis

To reveal valence states for the constituent elements (La, Ni, Sr, and O) in $La_{2-x}Sr_xNiO_4$, X-ray photoelectron spectroscopy (XPS) was used. The survey scan data for La_2NiO_4 are presented in Fig. 7(a), revealing particular peaks corresponding to the elements La (3d), Ni (2p), Sr (3d), and O (1s) only. To establish binding energies, the C 1s peak at 285 eV was employed as a reference. Core level spectra for Ni 2p, La 3d, Sr 3d, and O 1s are depicted in Fig. 7(b–e). These core level peaks were fitted using the Shirley function.

In Fig. 7(b), the XPS spectra of Ni for various compositions reveal two distinct peaks at 855.2 eV and 851.6 eV. These peaks can be attributed to the characteristic peaks of Ni $2p_{3/2}$ and the satellite peak, respectively. This observation suggests that the chemical state of nickel is predominantly Ni^{2+} in LN0, in agreement with previous reports.[6] However, for LN1 and LN2, the presence of Ni^{3+} is confirmed, as indicated by the presence of two peaks around 872 eV, corresponding to Ni^{3+} states. As Sr increases, the concentration of Ni^{3+} increases.

The XPS spectra of La 3d for LN0, LN1, and LN2 are presented in Fig. 7(c) and they primarily exhibit the spin–orbit splitting of La $3d_{5/2}$ and $3d_{3/2}$, as previously reported.[30] In the synthesized samples, the characteristic peaks of $3d_{5/2}$ are centered at 834.28 eV and 838.29 eV, while the peaks of $3d_{3/2}$ are located around 851.53 eV and 855.14 eV. These findings

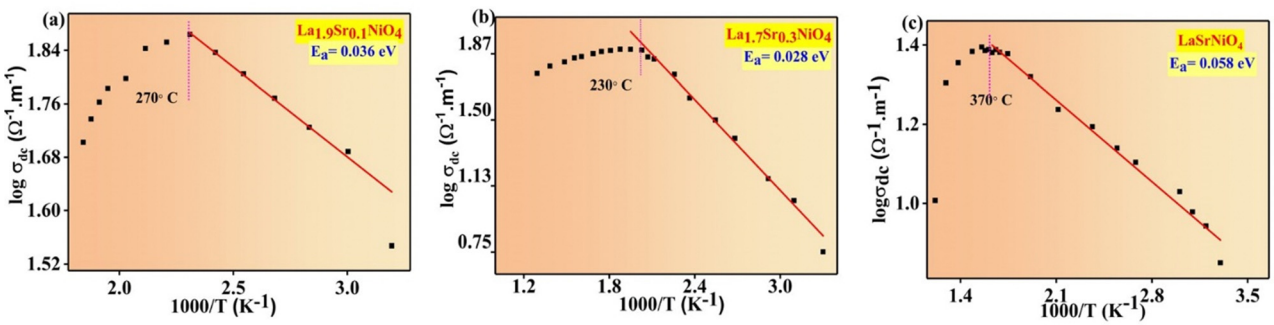

Fig. 6 (a–c) Variation of the logarithm of DC conductivity with the inverse of temperature. The activation energy (E_a) of the samples was calculated from the slope of the straight-line fit.

Published on 16 May 2024. Downloaded on 7/22/2025 2:32:36 PM.

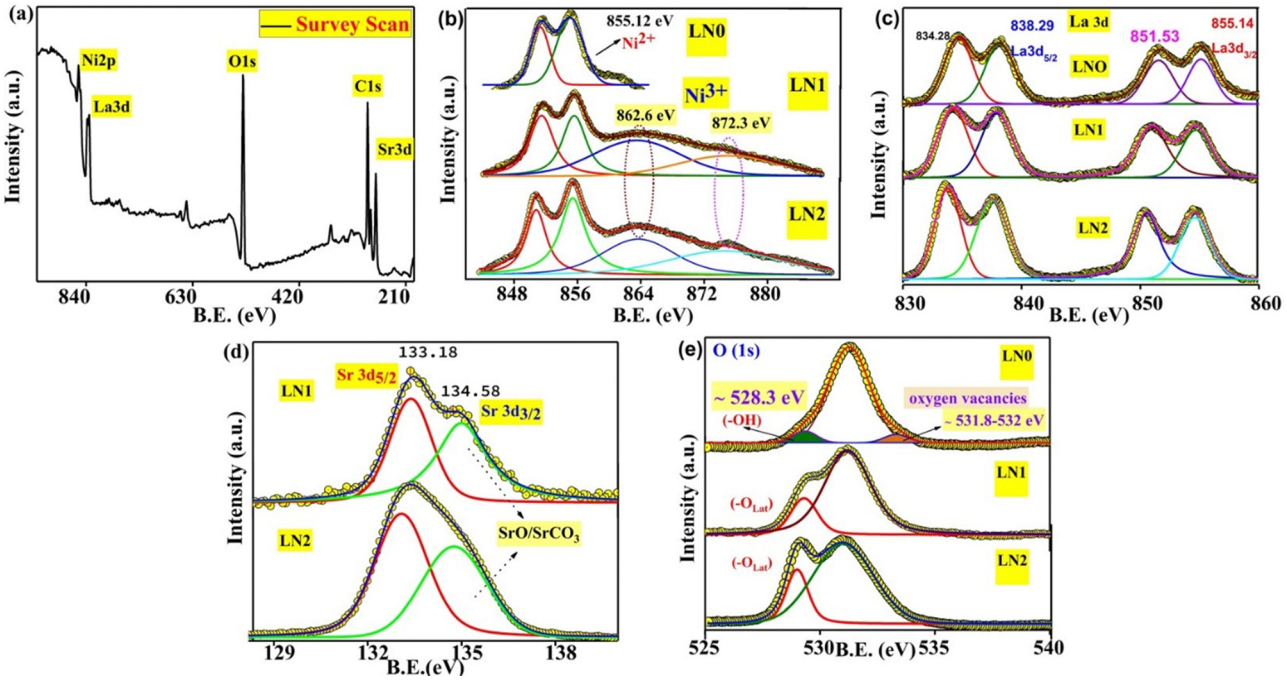

Fig. 7 The XPS spectrum: (a) survey scan, (b) core level spectra of Ni (2p), (c) core level spectra of La (3d), (d) core level spectra of Sr (3d), and (e) core level spectra of O (1s).

strongly suggest that lanthanum in all the samples is predominantly in the La^{3+} state.

The core–shell XPS spectrum of Sr 3d is shown in Fig. 7(d) and it mainly consists of the spin–orbit splitting of Sr 3d into Sr $3d_{5/2}$ and Sr $3d_{3/2}$ respectively. For both the samples LN1 and LN2, the representative peaks of Sr $3d_{5/2}$ are around 133 eV and for Sr $3d_{3/2}$ around 134 eV respectively confirming that the valence state of Sr is +2 in both the samples.[31]

Conversely, in the XPS spectra of O (1s) depicted in Fig. 7(e), a single peak is discerned, which can be further deconvoluted into three distinct peaks. These peaks have been attributed to different oxygen species. The lower binding energy peak, located at approximately 528.3 eV, corresponds to OH^- adsorption, whereas the peak at 531 eV belongs to lattice oxygen. The increase in the intensity of the peak corresponding to OH^- adsorption on increasing the concentration of Sr at 528 eV is because Sr^{2+} is more prone to OH^- adsorption than La^{3+}. These results show that charge compensation on doping Sr at the La site is occurring by conversion of a partial amount of Ni^{2+} into Ni^{3+} state, according to eqn (8).

7. Impedance analysis

The "reactance" is a key parameter that helps us understand the phase relationships between current and voltage when an alternating electric field is applied. Based on the sign of the reactant, we can differentiate a capacitor and an inductor. When voltage lags behind the current, we observe a negative reactance, indicating the capacitive nature of the material. Conversely, a positive reactance suggests inductive characteristics, where the current phase lags behind the voltage phase. This subtle polarity in reactance holds significance for comprehending and utilizing material electrical properties, making it relevant in various research and technological applications.[11,13,32,33]

There was a corresponding relation between permittivity and reactance:

$$\varepsilon' = -\frac{Z''}{2\prod f C_0[(Z'^2) + (Z''^2)]} \quad (9)$$

where Z' is the resistance, Z'' is the reactance, C_0 is the vacuum capacitance, and f is the test frequency.

Fig. 8(a) shows the frequency dependence of reactance for samples with different amounts of Sr-dopant at room temperature. The reactance displayed an escalating trend with the increase in frequency. For $La_{2-x}Sr_xNiO_4$ ceramics (where x varies from 0 to 1), it was observed that the reactance remained consistently positive across the entire range of test frequencies. Furthermore, the corresponding real permittivity exhibited a negative value, attributed to the occurrence of plasmonic oscillations. A similar behavior was observed by many researchers.[34]

Meanwhile, Fig. 8(b) gives the frequency dependence of the impedance phase angle for samples with different Sr-dopants. The positive phase angle suggests that the phase relationship between voltage and current in epsilon-negative samples is different from that in positive permittivity materials. With Sr-dopant increasing, the ceramics exhibit a higher phase angle.

As indicated in Fig. 8(c), the variation of Z'' with Z' also confirms that the reactance is positive. The value of Z' at the

 This journal is © The Royal Society of Chemistry 2024

Published on 16 May 2024. Downloaded on 7/22/2025 2:32:36 PM.

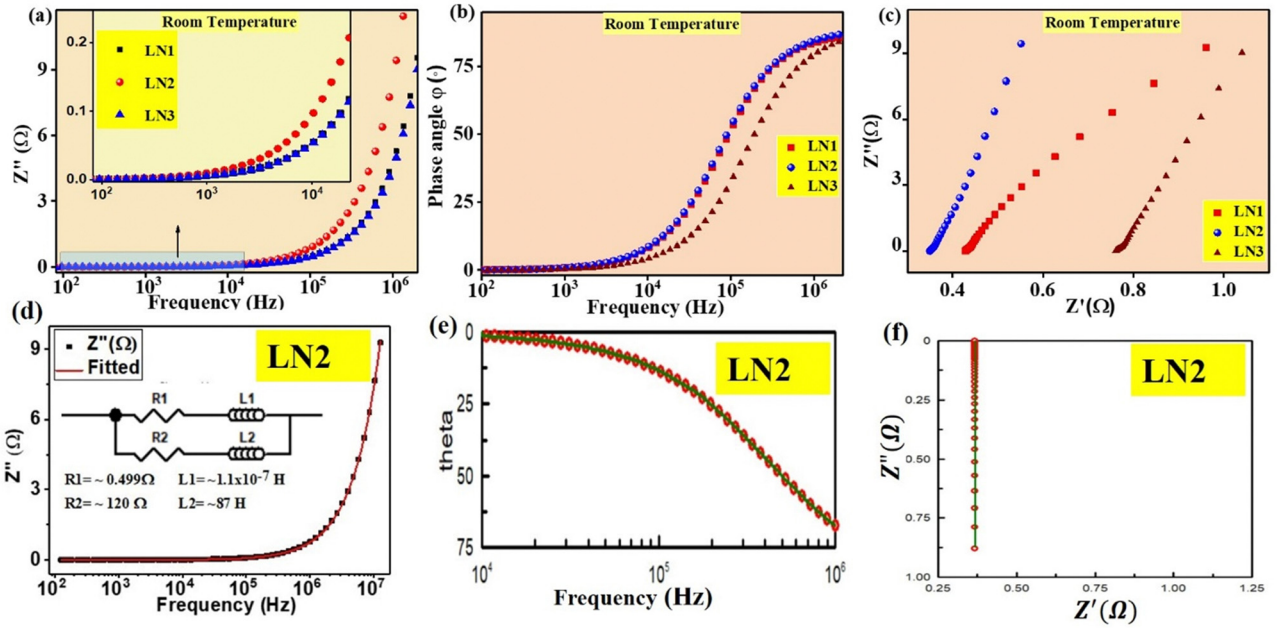

Fig. 8 The room temperature variation of (a) reactance (Z''). (b) Phase angle (Φ). With frequency (c) Z'' (reactance) *vs.* Z' (resistance). (d)–(f) Corresponding fitting of the experimental data for sample LN2.

lowest frequency (represented by the intercept on the *x*-axis) decreases as the Sr concentration increases. It is important to clarify that Z' signifies DC resistance, and this decrease in the value with increasing Sr concentration suggests that the samples are exhibiting a more pronounced inductive behavior. In other words, the inductive characteristic was responsible for negative permittivity from the perspective of impedance property.[11]

Here, it is important to note that the possibility of stray inductance provided by the sample holder and its connecting wires may unwittingly contribute to the experimentally observed impedance values since the total measured impedance values are small in magnitude. Therefore, it is necessary to take this into account and separate the unintentional contribution caused by the sample holder's impedance from experimentally collected data before analyzing the reactance behavior of the synthesized samples.

For this purpose, different combinations of resistors and inductors were tried to model and simulate the experimentally measured impedance data using *Z*-view simulation software. For sample LN2, the equivalent circuit as shown in the inset of Fig. 8(d) is found to be the most suitable circuit to represent the experimentally measured impedance data. Further, the obtained results were validated through complex fitting in Origin Pro17. In Fig. 8(d), the values of R1, R2, L1, and L2 were obtained from complex impedance data fitting of the equivalent circuit. Fig. 8(e and f) is the simulated version of the same data using *Z*-View software.

For other samples, similar processes were used and the findings are summarized in Table 5. It is observed that the values of R1 and L1 are very small compared to R2 and L2 values. Therefore we have assigned R1 and L1 to the contribution from the wires and sample holder and R2 and L2 to the contributions from our samples. Negative dielectric behavior is caused by plasmonic oscillations of free charge carriers. The plasmonic oscillation of these charge carriers in an applied sinusoidal electric field gives rise to surface current. The origin of the sample's inductive behavior (L2) can be attributed to this current on the surface of the sample. The resistance (R2) can be attributed to the resistance offered to this circulating current on the grains' surface and/or resistance offered to the conduction current within/through the grains.

Table 5 Values obtained from complex fitting of the impedance data for various compositions

Sample	R1 (mΩ)	L1 (μH)	R2 (Ω)	L2 (H)
LN1	4.23	10	191	62
LN2	4.17	11	120	87
LN3	4.11	11	147	23

Furthermore, our materials with negative permittivity offer significantly higher inductance (~87 H) compared to conventional wire-wound inductors. Therefore, exploring negative permittivity materials holds great research potential for developing coil-less electric inductors.[35]

8. Microwave shielding effectiveness analysis

The effectiveness of electromagnetic interference (EMI) shielding relies on three primary mechanisms: reflection, absorption,

Published on 16 May 2024. Downloaded on 7/22/2025 2:32:36 PM.

and multiple internal reflection.[36] EMI shields primarily reflect radiation, utilizing charge carriers that interact with EM fields, thus requiring high electrical conductivity. Absorption of electromagnetic radiation is facilitated by interactions with electric/magnetic dipoles, electrons, and phonons. Multiple internal reflections within the material significantly contribute to EMI shielding effectiveness, stemming from scattering centers, interfaces, or defect sites, resulting in multiple scattering and EM wave absorption. The total shielding effectiveness (SE_T) includes shielding due to reflection (SE_R) arising from an impedance mismatch between air and the shielding material, while shielding due to absorption (SE_A) dissipates electromagnetic microwaves in the shield. The absorption of EM energy (SE_M) correlates with multiple internal reflections.

The total shielding effectiveness (SE_T) would be given by[37]

$$SE_T = SE_A + SE_R + SE_M \quad (10)$$

When the total shielding effectiveness of the material is more than 10 dB, then loss due to multiple reflections (SE_M) becomes negligible and can be neglected.[38]

Thus, the total shielding effectiveness (SE_T) now can be expressed as

$$SE_T = SE_A + SE_R \quad (11)$$

where SE_A and SE_R can be directly calculated by the *S*-parameters obtained from the two-port VNA measurement.[38,39]

$$SE_A = 10\log\left(\frac{10^{\frac{S21}{10}}}{1-10^{\frac{S11}{10}}}\right) \quad (12)$$

$$SE_R = 10\log\left(1-10^{\frac{S11}{10}}\right) \quad (13)$$

Fig. 9(a) represents the material under test (MUT). Fig. 9(b–d) illustrates the variation of different microwave shielding parameters SE_R, SE_A, and SE_T in the frequency range of 8–13 GHz. Fig. 9(b) reveals that the reflection phenomena dominate the shielding mechanism. The total shielding effectiveness (SE_T) is approximately −15 dB for sample LN0 and about −47 dB for sample LN2, *i.e.* 99.99% microwave absorption at 8.54 GHz with a matching thickness of only 2 mm, which is higher than previously reported data.[18]

This increase in SE_R or the total effective shielding parameter, SE_T (=SE_A + SE_R), for the LN2 sample in comparison with LN0 may be attributed to the higher conductivity, resulting from the presence of higher density of plasmons (surface delocalized electrons). The high conductivity of the material results in a significant impedance mismatch with the

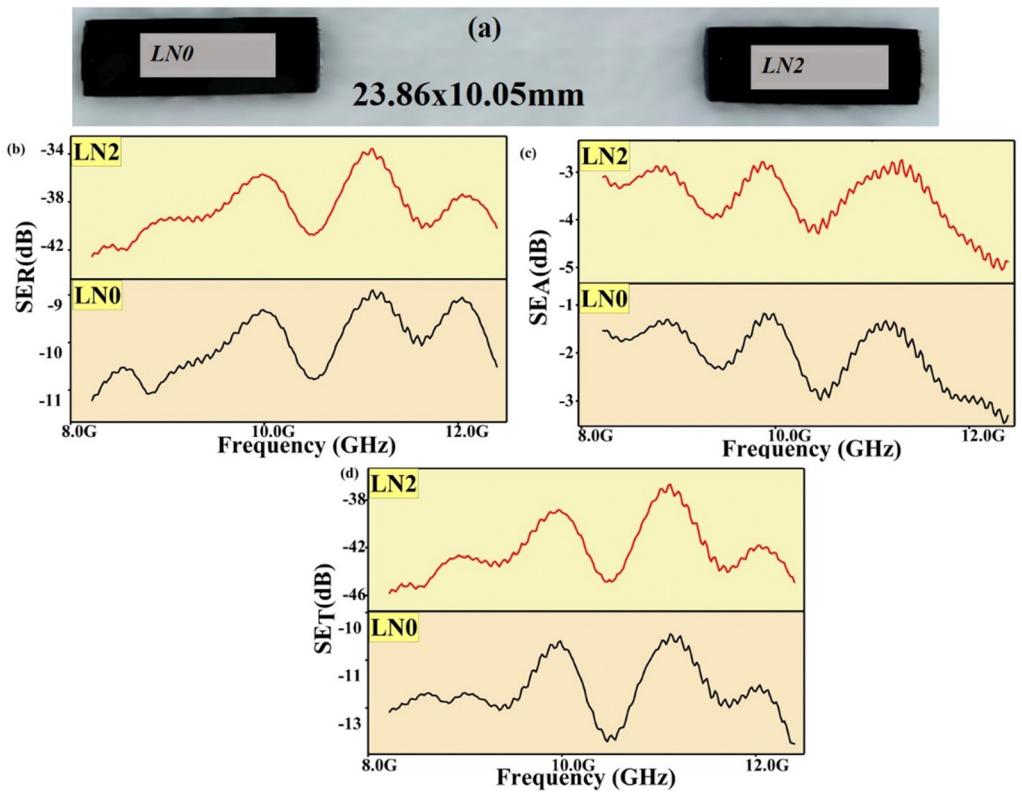

Fig. 9 Schematic diagram of sample dimension used for measuring *S*-parameters in the GHz range (8–13 GHz). Variation of (b) shielding effectiveness due to reflection (SE_R), (c) shielding effectiveness due to absorption (SE_A), and (d) the total shielding effectiveness parameters (SE_T) with frequency.

 This journal is © The Royal Society of Chemistry 2024

Published on 16 May 2024. Downloaded on 7/22/2025 2:32:36 PM.

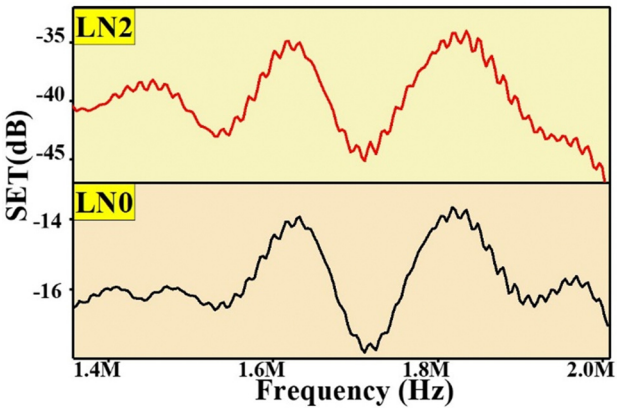

Fig. 10 Variation of total microwave shielding effectiveness (SET) with frequency (1–2 MHz) of LN0 and LN2 samples.

surrounding air,[25] and reduces the skin depth $\left(\delta = \sqrt{\frac{2}{\omega\mu\sigma}}\right)$ of the material. The combination of high impedance mismatch at the interface with incident electromagnetic fields and reduced skin depth enhances the material's ability to effectively reflect and attenuate microwave radiation.

Similarly, to provide an inclusive understanding of the shielding effectiveness of the samples at lower frequencies as well, Fig. 10 further examines their total shielding effectiveness in the 1–2 MHz region. SE_T for sample LN0 is about −11 dB to −15 dB and for LN2 is between −41 and −45 dB. These frequency ranges are crucial for assessing the effectiveness of the shield in practical electromagnetic interference shield developments.

It is important to mention that the desired EMI shielding effectiveness for commercial applications is approximately 20 dB, which corresponds to equal to or less than 1% transmittance of electromagnetic waves. Hence, there is an expectation that our improved material could be more suitable for various commercial applications.

9. Conclusion

In this paper, we have tried to establish the correlation between electrical conductivity and negative dielectric constant. Single-phase Sr-doped La_2NiO_4 was successfully synthesized using the solid-state reaction method. Examination of the SEM image verified the irregular growth of cuboidal-shaped grains. The real part of permittivity consistently exhibited negative values across all tested frequencies and temperatures. The experimental data points were well-fitted by the Drude model, and this negative permittivity behavior was attributed to the plasma oscillation of free charge carriers. The lower activation energy (E_a) for DC conduction indicated a small polaron hopping conduction mechanism. Positive values of the imaginary part of impedance (Z'') confirmed inductive behavior across the entire range of temperature and frequency measurements. The microwave studies indicate a prominent rise in total shielding effectiveness (SE_T) upon the incorporation of Sr (LN2) compared to the undoped sample (LN0).

It can be inferred from the observations that a higher magnitude of electrical conductivity leads to a larger negative permittivity, which in turn causes a stronger impedance mismatch. This results in an increase in the total shielding effectiveness (SE_T) value of the samples. This outcome signifies the potential to tune and modify the microwave shielding properties by compositional modification for a variety of applications.

Data availability

The raw/processed data required to reproduce these findings cannot be shared at this time as the data also form part of an ongoing study.

Conflicts of interest

The authors declare that they have no known competing financial interests or personal relationships that could have appeared to influence the work reported in this paper.

Acknowledgements

The authors are grateful to the Head, Department of Physics, and the Coordinator, CIFC, IIT(BHU), Varanasi, for providing experimental facilities. The author Mr Tarun Katheriya is also thankful to the Ministry of Education and the Council of Scientific & Industrial Research (CSIR) for the fellowship to carry out this work, which are bodies of the Government of India, New Delhi, India.

References

1 V. G. Veselago, *Phys.-Usp.*, 1968, **10**, 509–514.
2 P. Xie, Z. Shi, M. Feng, K. Sun, Y. Liu, K. Yan, C. Liu, T. A. A. Moussa, M. Huang, S. Meng, G. Liang, H. Hou, R. Fan and Z. Guo, *Adv. Compos. Hybrid Mater.*, 2022, **5**, 679–695.
3 G. Fan, P. Xie, Z. Wang, Y. Qu, Z. Zhang, Y. Liu and R. Fan, *Ceram. Int.*, 2017, **43**, 16980–16985.
4 K. L. Yan, R. H. Fan, M. Chen, K. Sun, L. W. Yin, H. Li, S. B. Pan and M. X. Yu, *J. Alloys Compd.*, 2015, **628**, 429–432.
5 G. Fan, K. Sun, Q. Hou, Z. Wang, Y. Liu and R. Fan, *EPJ Appl. Metamater.*, 2021, **8**, DOI: 10.1051/epjam/2021005.
6 X. Ye, S. Dong, X. Jin, J. Wei, L. Wang and Y. Zhang, *Coatings*, 2022, **12**, DOI: 10.3390/coatings12111739.
7 K. Sun, P. Yang, Q. He, R. Fan, Z. Wang, J. Tian, X. Yang, W. Duan, X. Wu and Z. Wang, *Ceram. Int.*, 2022, **48**, 8417–8422.
8 K. Yan, L. Shen, R. Fan and N. Bao, *J. Mater. Sci.*, 2021, **56**, 10183–10190.
9 G. Nirala, D. Yadav, T. Katheriya and S. Upadhyay, *J. Eur. Ceram. Soc.*, 2022, **42**, 453–461.
10 S. Mno, *J. Mater. Sci.*, 2022, **57**, 15862–15875.

Published on 16 May 2024. Downloaded on 7/22/2025 2:32:36 PM.

11 G. Fan, Z. Wang, K. Sun, Y. Liu and R. Fan, *J. Mater. Chem. C*, 2020, **8**, 11610–11617.
12 G. Fan, Z. Wang, K. Sun, Y. Liu and R. Fan, *J. Mater. Sci. Technol.*, 2021, **61**, 125–131.
13 T. Katheriya and S. Upadhyay, *Phys. Scr.*, 2023, **98**, DOI: 10.1088/1402-4896/acf967.
14 V. V. Kharton, A. P. Viskup, E. N. Naumovich and F. M. B. Marques, *J. Mater.*, 1999, **9**, 2623–2629.
15 V. V. Vashook, I. I. Yushkevich, L. V. Kokhanovsky, L. V. Makhnach, S. P. Tolochko, I. F. Kononyuk, H. Ullmann and H. Altenburg, *Solid State Ionics*, 1999, **119**, 23–30.
16 K. Zakharchuk, A. Bamburov, E. N. Naumovich, M. A. Vieira and A. A. Yaremchenko, *Processes*, 2021, **10**, 82.
17 A. R. Gilev, E. A. Kiselev, D. M. Zakharov and V. A. Cherepanov, *J. Alloys Compd.*, 2018, **753**, 491–501.
18 S. Liu, Y. Cheng, J. He, S. Yan, H. Luo and L. Deng, *Front. Mater.*, 2020, **7**, DOI: 10.3389/fmats.2020.00271.
19 M. Saleem, D. Singh, A. Mishra and D. Varshney, *Mater. Res. Express*, 2018, **6**, DOI: 10.1088/2053-1591/aaecf7.
20 K. Zakharchuk, A. Kovalevsky and A. Yaremchenko, *Materials*, 2023, **6**(4), 1755.
21 G. Nirala, D. Yadav and S. Upadhyay, *J. Adv. Ceram.*, 2020, **9**, 129–148.
22 P. Drude, *Ann. Phys.*, 1900, **306**, 566–613.
23 X. Yao, X. Kou, J. Qiu and M. Moloney, *J. Phys. Chem. C*, 2016, **120**, 4937–4944.
24 C. Cheng, K. Yan, R. Fan, L. Qian, Z. Zhang, K. Sun and M. Chen, *Carbon*, 2016, **96**, 678–684.
25 C. Cheng, R. Fan, Z. Wang, Q. Shao, X. Guo, P. Xie, Y. Yin, Y. Zhang, L. An, Y. Lei, J. E. Ryu, A. Shankar and Z. Guo, *Carbon*, 2017, **125**, 103–112.
26 K. Ishikawa, W. Shibata, K. Watanabe, T. Isonaga, M. Hashimoto and Y. Suzuki, *J. Solid State Chem.*, 1997, **131**, 275–281.
27 W.-H. Jung, *J. Mater.*, 2013, 1–6.
28 X. Ma, Y. Gao, B. Yang, X. Lou, J. Huang, L. Ma and D. Jing, *Nanoscale*, 2022, 7083–7095.
29 D. H. Hop, R. B. K. Chung, Y. W. Heo, J. J. Kim and J. H. Lee, *J. Korean Ceram. Soc.*, 2020, **57**, 416–422.
30 P. Swetha, R. Aswini, M. Binesh, M. S. Muhammed, K. Sridharan and S. Swaminathan, *Mater. Today Commun.*, 2023, **34**, 105287.
31 J. L. Ortiz-Quiñonez, L. García-González, F. E. Cancino-Gordillo and U. Pal, *Mater. Chem. Phys.*, 2020, **246**, DOI: 10.1016/j.matchemphys.2020.122834.
32 Z. Wei, Z. Wang, G. Fan, C. Xu, G. Shi, G. Zhang, Y. Liu and R. Fan, *Ceram. Int.*, 2021, **47**, 2208–2213.
33 C. Deng, Y. Li, H. Wang, Y. Qu, X. Qi, Z. Peng, Z. Chen, H. Shen, K. Sun and R. Fan, *Ceram. Int.*, 2023, **49**, 16149–16155.
34 Y. Wu, Z. Wang, X. Liu, X. Shen, Q. Zheng, Q. Xue and J. K. Kim, *ACS Appl. Mater. Interfaces*, 2017, **9**, 9059–9069.
35 G. Nirala, T. Katheriya, D. Yadav, H. Verma and S. Upadhyay, *Emergent Mater.*, 2023, **6**, 1951–1962.
36 G. Kulkarni, P. Kandesar, N. Velhal, V. Phadtare, A. Jatratkar, S. K. Shinde, D. Y. Kim and V. Puri, *Chem. Eng. J.*, 2019, **355**, 196–207.
37 S. W. Phang, T. Hino, M. H. Abdullah and N. Kuramoto, *Mater. Chem. Phys.*, 2007, **104**, 327–335.
38 T. K. Gupta, B. P. Singh, V. N. Singh, S. Teotia, A. P. Singh, I. Elizabeth, S. R. Dhakate, S. K. Dhawan and R. B. Mathur, *J. Mater. Chem. A*, 2014, **2**, 4256–4263.
39 C. Y. Tsay, Y. H. Huang and D. S. Hung, *Ceram. Int.*, 2014, **40**, 3947–3951.

This journal is © The Royal Society of Chemistry 2024